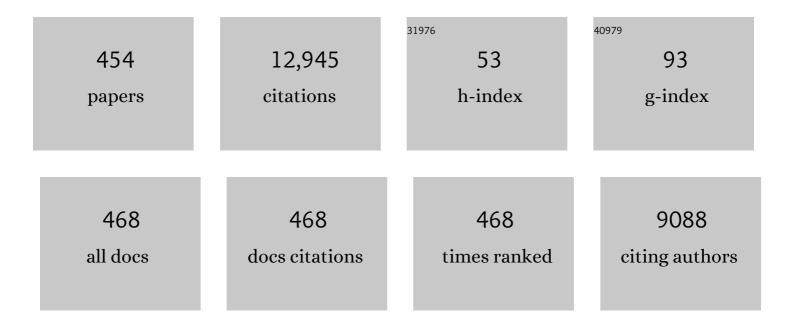
List of Publications by Year in descending order

Source: https://exaly.com/author-pdf/8416184/publications.pdf Version: 2024-02-01



#	Article	IF	CITATIONS
1	Comet 81P/Wild 2 Under a Microscope. Science, 2006, 314, 1711-1716.	12.6	848
2	The Rubble-Pile Asteroid Itokawa as Observed by Hayabusa. Science, 2006, 312, 1330-1334.	12.6	761
3	Three-Dimensional Structure of Hayabusa Samples: Origin and Evolution of Itokawa Regolith. Science, 2011, 333, 1125-1128.	12.6	249
4	Low Core-Mantle Boundary Temperature Inferred from the Solidus of Pyrolite. Science, 2014, 343, 522-525.	12.6	224
5	Chondrulelike Objects in Short-Period Comet 81P/Wild 2. Science, 2008, 321, 1664-1667.	12.6	215
6	Elemental Compositions of Comet 81P/Wild 2 Samples Collected by Stardust. Science, 2006, 314, 1731-1735.	12.6	200
7	Establishing Functional Residual Capacity at Birth: The Effect of Sustained Inflation and Positive End-Expiratory Pressure in a Preterm Rabbit Model. Pediatric Research, 2009, 65, 537-541.	2.3	178
8	Imaging lung aeration and lung liquid clearance at birth. FASEB Journal, 2007, 21, 3329-3337.	0.5	177
9	Growth behavior of hydrogen micropores in aluminum alloys during high-temperature exposure. Acta Materialia, 2009, 57, 2277-2290.	7.9	150
10	3D Shape Characterization and Image-Based DEM Simulation of the Lunar Soil Simulant FJS-1. Journal of Aerospace Engineering, 2009, 22, 15-23.	1.4	141
11	Effect of Sustained Inflation Length on Establishing Functional Residual Capacity at Birth in Ventilated Premature Rabbits. Pediatric Research, 2009, 66, 295-300.	2.3	141
12	2D and 3D X-ray phase retrieval of multi-material objects using a single defocus distance. Optics Express, 2010, 18, 6423.	3.4	141
13	Preliminary analysis of the Hayabusa2 samples returned from C-type asteroid Ryugu. Nature Astronomy, 2022, 6, 214-220.	10.1	136
14	Positive end-expiratory pressure enhances development of a functional residual capacity in preterm rabbits ventilated from birth. Journal of Applied Physiology, 2009, 106, 1487-1493.	2.5	134
15	The role of trace element segregation in the eutectic modification of hypoeutectic Al–Si alloys. Journal of Alloys and Compounds, 2010, 489, 415-420.	5.5	132
16	On the origin of speckle in x-ray phase contrast images of lung tissue. Physics in Medicine and Biology, 2004, 49, 4335-4348.	3.0	129
17	Electron density measurement with dual-energy x-ray CT using synchrotron radiation. Physics in Medicine and Biology, 2003, 48, 673-685.	3.0	122
18	The influence of Ni and Zn additions on microstructure and phase transformations in Sn–0.7Cu/Cu solder joints. Acta Materialia, 2015, 83, 357-371.	7.9	119

#	Article	IF	CITATIONS
19	High-density three-dimensional mapping of internal strain by tracking microstructural features. Acta Materialia, 2008, 56, 2167-2181.	7.9	117
20	Processing of a Strong Biodegradable Poly[(R)-3-hydroxybutyrate] Fiber and a New Fiber Structure Revealed by Micro-Beam X-Ray Diffraction with Synchrotron Radiation. Macromolecular Rapid Communications, 2004, 25, 1100-1104.	3.9	111
21	Magma deformation may induce non-explosive volcanism via degassing through bubble networks. Earth and Planetary Science Letters, 2009, 281, 267-274.	4.4	110
22	Dynamic imaging of the lungs using x-ray phase contrast. Physics in Medicine and Biology, 2005, 50, 5031-5040.	3.0	104
23	Inspiration regulates the rate and temporal pattern of lung liquid clearance and lung aeration at birth. Journal of Applied Physiology, 2009, 106, 1888-1895.	2.5	100
24	Development of X-ray Imaging for Observing Solidification of Carbon Steels. ISIJ International, 2011, 51, 402-408.	1.4	100
25	Formation of Highly Ordered Structure in Poly[(R)-3-hydroxybutyrate-co-(R)-3-hydroxyvalerate] High-Strength Fibers. Macromolecules, 2006, 39, 2940-2946.	4.8	94
26	Quantitative assessment of microstructure and its effects on compression behavior of aluminum foams via high-resolution synchrotron X-ray tomography. Metallurgical and Materials Transactions A: Physical Metallurgy and Materials Science, 2006, 37, 1211-1219.	2.2	93
27	Healing behavior of preexisting hydrogen micropores in aluminum alloys during plastic deformation. Acta Materialia, 2009, 57, 4391-4403.	7.9	93
28	The True Origin of Ductile Fracture in Aluminum Alloys. Metallurgical and Materials Transactions A: Physical Metallurgy and Materials Science, 2014, 45, 765-776.	2.2	91
29	Granular deformation mechanisms in semi-solid alloys. Acta Materialia, 2011, 59, 4933-4943.	7.9	89
30	Direct measurement procedure for three-dimensional local crack driving force using synchrotron X-ray microtomography. Acta Materialia, 2008, 56, 6027-6039.	7.9	88
31	CT dose reduction factors in the thousands using X-ray phase contrast. Scientific Reports, 2017, 7, 15953.	3.3	88
32	Evolution of bubble microstructure in sheared rhyolite: Formation of a channelâ€like bubble network. Journal of Geophysical Research, 2008, 113, .	3.3	86
33	Development of high spatial resolution X-ray CT system at BL47XU in SPring-8. Nuclear Instruments and Methods in Physics Research, Section A: Accelerators, Spectrometers, Detectors and Associated Equipment, 2001, 467-468, 853-856.	1.6	85
34	Dynamic measures of regional lung air volume using phase contrast x-ray imaging. Physics in Medicine and Biology, 2008, 53, 6065-6077.	3.0	83
35	Phase contrast X-ray imaging of mice and rabbit lungs: a comparative study. British Journal of Radiology, 2005, 78, 1018-1027.	2.2	81
36	<i>In situ</i> observation of solidification phenomena in Al–Cu and Fe–Si–Al alloys. International Journal of Cast Metals Research, 2009, 22, 15-21.	1.0	81

#	Article	IF	CITATIONS
37	Direct observation of deformation in semi-solid carbon steel. Scripta Materialia, 2011, 64, 1129-1132.	5.2	81
38	X-ray refraction-enhanced imaging and a method for phase retrieval for a simple object. Journal of Synchrotron Radiation, 2002, 9, 160-165.	2.4	80
39	Shear deformation experiments on vesicular rhyolite: Implications for brittle fracturing, degassing, and compaction of magmas in volcanic conduits. Journal of Geophysical Research, 2010, 115, .	3.3	80
40	Microbeam X-ray Diffraction and Enzymatic Degradation of Poly[(R)-3-hydroxybutyrate] Fibers with Two Kinds of Molecular Conformations. Macromolecules, 2006, 39, 5789-5795.	4.8	78
41	Dendrite fragmentation induced by massive-like δ–γ transformation in Fe–C alloys. Nature Communications, 2019, 10, 3183.	12.8	65
42	Construction and Commissioning of A 248 m-long Beamline with X-ray Undulator Light Source. AIP Conference Proceedings, 2004, , .	0.4	64
43	IMAGING LUNG AERATION AND LUNG LIQUID CLEARANCE AT BIRTH USING PHASE CONTRAST Xâ€RAY IMAGING. Clinical and Experimental Pharmacology and Physiology, 2009, 36, 117-125.	1.9	64
44	Influence of high-temperature solution treatments on mechanical properties of an Al–Si–Cu aluminum alloy. Acta Materialia, 2010, 58, 2014-2025.	7.9	64
45	Non-destructive observation of internal fatigue crack growth in Ti–6Al–4V by using synchrotron radiation μCT imaging. International Journal of Fatigue, 2016, 93, 397-405.	5.7	64
46	Three-dimensional fatigue crack growth behavior in an aluminum alloy investigated with in situ high-resolution synchrotron X-ray microtomography. Acta Materialia, 2009, 57, 3287-3300.	7.9	63
47	4D Visualization of a Cathode Catalyst Layer in a Polymer Electrolyte Fuel Cell by 3D Laminography–XAFS. Angewandte Chemie - International Edition, 2012, 51, 10311-10314.	13.8	63
48	Coupled effect of magma degassing and rheology on silicic volcanism. Earth and Planetary Science Letters, 2013, 362, 163-170.	4.4	63
49	Assessment of hydrogen embrittlement via image-based techniques in Al–Zn–Mg–Cu aluminum alloys. Acta Materialia, 2019, 176, 96-108.	7.9	63
50	Quantitative evaluation of attenuation contrast of X-ray computed tomography images using monochromatized beams. American Mineralogist, 2005, 90, 132-142.	1.9	61
51	Three-dimensional diffusion of non-sorbing species in porous sandstone: computer simulation based on X-ray microtomography using synchrotron radiation. Journal of Contaminant Hydrology, 2004, 74, 253-264.	3.3	58
52	Optical Properties of In Situ Eye Lenses Measured with X-Ray Talbot Interferometry: A Novel Measure of Growth Processes. PLoS ONE, 2011, 6, e25140.	2.5	57
53	In situ investigation of unidirectional solidification in Sn–0.7Cu and Sn–0.7Cu–0.06Ni. Acta Materialia, 2011, 59, 4043-4054.	7.9	56
54	Analytical dual-energy microtomography: A new method for obtaining three-dimensional mineral phase images and its application to Hayabusa samples. Geochimica Et Cosmochimica Acta, 2013, 116, 5-16.	3.9	55

#	Article	IF	CITATIONS
55	Influence of hydrogen on strain localization and fracture behavior in Al Zn Mg Cu aluminum alloys. Acta Materialia, 2018, 159, 332-343.	7.9	55
56	Highâ€resolution visualization of airspace structures in intact mice via synchrotron phaseâ€contrast Xâ€ray imaging (PCXI). Journal of Anatomy, 2008, 213, 217-227.	1.5	54
57	Robust Liquid Marbles Stabilized with Surface-Modified Halloysite Nanotubes. Langmuir, 2013, 29, 14971-14975.	3.5	51
58	Combined microtomography, thermal desorption spectroscopy, X-ray diffraction study of hydrogen trapping behavior in 7XXX aluminum alloys. Materials Science & Engineering A: Structural Materials: Properties, Microstructure and Processing, 2016, 655, 221-228.	5.6	51
59	Submicrometer-resolution three-dimensional imaging with hard x-ray imaging microtomography. Review of Scientific Instruments, 2002, 73, 4246-4249.	1.3	50
60	Characterization of two-dimensional ultra-small-angle X-ray scattering apparatus for application to rubber filled with spherical silica under elongation. Journal of Applied Crystallography, 2007, 40, s397-s401.	4.5	50
61	<i>In situ</i> observation of water distribution and behaviour in a polymer electrolyte fuel cell by synchrotron X-ray imaging. Journal of Synchrotron Radiation, 2008, 15, 329-334.	2.4	50
62	Damage micromechanisms in dual-phase steel investigated with combined phase- and absorption-contrast tomography. Acta Materialia, 2017, 126, 401-412.	7.9	50
63	Three-dimensional observation of nanoscopic precipitates in an aluminum alloy by microtomography with Fresnel zone plate optics. Applied Physics Letters, 2006, 89, 143112.	3.3	49
64	<i>In situ</i> observation of nucleation, fragmentation and microstructure evolution in Sn–Bi and Al–Cu alloys. International Journal of Cast Metals Research, 2008, 21, 125-128.	1.0	48
65	Threeâ€dimensional microstructure of samples recovered from asteroid 25143 Itokawa: Comparison with <scp>LL</scp> 5 and <scp>LL</scp> 6 chondrite particles. Meteoritics and Planetary Science, 2014, 49, 172-187.	1.6	48
66	Computed tomography imaging of the neuronal structure ofDrosophilabrain. Journal of Synchrotron Radiation, 2007, 14, 282-287.	2.4	47
67	Bulk mineralogy and threeâ€dimensional structures of individual Stardust particles deduced from synchrotron Xâ€ray diffraction and microtomography analysis. Meteoritics and Planetary Science, 2008, 43, 247-259.	1.6	47
68	Floral Evidence of Annonaceae from the Late Cretaceous of Japan. International Journal of Plant Sciences, 2008, 169, 908-917.	1.3	47
69	Murine pulmonary acinar mechanics during quasi-static inflation using synchrotron refraction-enhanced computed tomography. Journal of Applied Physiology, 2013, 115, 219-228.	2.5	47
70	Bone structure and mineralization demonstrated using synchrotron radiation computed tomography (SR-CT) in animal models: preliminary findings. Journal of Bone and Mineral Metabolism, 2003, 21, 287-293.	2.7	46
71	Application of synchrotron x-ray microtomography to investigate ductile fracture in Al alloys. Applied Physics Letters, 2005, 87, 241907.	3.3	46
72	The eye lens: age-related trends and individual variations in refractive index and shape parameters. Oncotarget, 2015, 6, 30532-30544.	1.8	46

#	Article	IF	CITATIONS
73	Origin and formation of iron silicide phases in the aerogel of the Stardust mission. Meteoritics and Planetary Science, 2008, 43, 121-134.	1.6	45
74	A method for estimating spatial resolution of real image in the Fourier domain. Journal of Microscopy, 2016, 261, 57-66.	1.8	45
75	Age-related changes in eye lens biomechanics, morphology, refractive index and transparency. Aging, 2019, 11, 12497-12531.	3.1	44
76	Structure investigation of narrow banded spherulites in polyhydroxyalkanoates by microbeam X-ray diffraction with synchrotron radiation. Polymer, 2005, 46, 5673-5679.	3.8	43
77	Monochromatic synchrotron radiation μCT reveals disuse-mediated canal network rarefaction in cortical bone of growing rat tibiae. Journal of Applied Physiology, 2006, 100, 274-280.	2.5	43
78	Development of high-resolution 4D <i>in vivo</i> -CT for visualization of cardiac and respiratory deformations of small animals. Physics in Medicine and Biology, 2008, 53, 4285-4301.	3.0	43
79	Phase contrast image segmentation using a Laue analyser crystal. Physics in Medicine and Biology, 2011, 56, 515-534.	3.0	42
80	Comparison of lens- and fiber-coupled CCD detectorsÂfor X-ray computed tomography. Journal of Synchrotron Radiation, 2011, 18, 217-223.	2.4	42
81	Statistical assessment of fatigue crack initiation from sub-surface hydrogen micropores in high-quality die-cast aluminum. Acta Materialia, 2011, 59, 4990-4998.	7.9	42
82	The role of lung inflation and sodium transport in airway liquid clearance during lung aeration in newborn rabbits. Pediatric Research, 2013, 73, 443-449.	2.3	41
83	Roles of Pre-Existing Hydrogen Micropores on Ductile Fracture. Materials Transactions, 2009, 50, 2285-2290.	1.2	39
84	Demonstration of osmotically dependent promotion of aerenchyma formation at different levels in the primary roots of rice using a †̃sandwich' method and X-ray computed tomography. Annals of Botany, 2012, 110, 503-509.	2.9	39
85	In situ phase contrast X-ray brain CT. Scientific Reports, 2018, 8, 11412.	3.3	39
86	Pressure and Composition Effects on Sound Velocity and Density of Coreâ€Forming Liquids: Implication to Core Compositions of Terrestrial Planets. Journal of Geophysical Research E: Planets, 2019, 124, 2272-2293.	3.6	39
87	Micro- and macrobehavior of granitic rock: observations and viscoelastic homogenization analysis. Computer Methods in Applied Mechanics and Engineering, 2001, 191, 47-72.	6.6	38
88	Massive transformation from <i>l̂´</i> phase to <i>l̂³</i> phase in Fe–C alloys and strain induced in solidifying shell. IOP Conference Series: Materials Science and Engineering, 2012, 33, 012036.	0.6	38
89	Direct observation of grain rotations during coarsening of a semisolid Al–Cu alloy. Proceedings of the United States of America, 2016, 113, E5998-E6006.	7.1	38
90	Initiation and growth behaviour of small internal fatigue cracks in Tiâ€6Alâ€4V via synchrotron radiation microcomputed tomography. Fatigue and Fracture of Engineering Materials and Structures, 2019, 42, 2093-2105.	3.4	38

#	Article	IF	CITATIONS
91	Surfactant Increases the Uniformity of Lung Aeration at Birth in Ventilated Preterm Rabbits. Pediatric Research, 2011, 70, 50-55.	2.3	37
92	Influences of hydrogen on deformation and fracture behaviors of high Zn 7XXX aluminum alloys. International Journal of Fracture, 2016, 200, 13-29.	2.2	37
93	Preferential penetration path of gallium into grain boundary in practical aluminium alloy. Philosophical Magazine, 2006, 86, 4351-4366.	1.6	36
94	Development of fast and high throughput tomography using CMOS image detector at SPring-8. Proceedings of SPIE, 2012, , .	0.8	36
95	Surface and internal structures of a space-weathered rim of an Itokawa regolith particle. Icarus, 2015, 257, 230-238.	2.5	36
96	Nondestructive three-dimensional element-concentration mapping of a Cs-doped partially molten granite by X-ray computed tomography using synchrotron radiation. American Mineralogist, 2004, 89, 1304-1313.	1.9	35
97	Development of micro-tomography system with Fresnel zone plate optics at SPring-8. , 2006, , .		35
98	Zernike phase-contrast x-ray microscope with pseudo-Kohler illumination generated by sectored (polygon) condenser plate. Journal of Physics: Conference Series, 2009, 186, 012020.	0.4	35
99	Microtomographic Analysis of Neuronal Circuits of Human Brain. Cerebral Cortex, 2010, 20, 1739-1748.	2.9	35
100	Phase-contrast X-ray microtomography of mouse fetus. Biology Open, 2012, 1, 269-274.	1.2	34
101	Study of creep cavitation behavior in tempered martensitic steel using synchrotron micro-tomography and serial sectioning techniques. Materials Science & Engineering A: Structural Materials: Properties, Microstructure and Processing, 2013, 564, 525-538.	5.6	34
102	Real time synchrotron X-ray observations of solidification in hypoeutectic Al–Si alloys. Materials Characterization, 2013, 85, 134-140.	4.4	34
103	Selection and constraint underlie irreversibility of tooth loss in cypriniform fishes. Proceedings of the National Academy of Sciences of the United States of America, 2014, 111, 7707-7712.	7.1	34
104	X-ray phase, absorption and scatter retrieval using two or more phase contrast images. Optics Express, 2010, 18, 19994.	3.4	33
105	Discovery of fossil asteroidal ice in primitive meteorite Acfer 094. Science Advances, 2019, 5, eaax5078.	10.3	33
106	Direct Observation and Image-Based Simulation of Three-Dimensional Tortuous Crack Evolution inside Opaque Materials. Physical Review Letters, 2008, 100, 115505.	7.8	32
107	Cavitation during high-temperature deformation in Al–Mg alloys. Acta Materialia, 2013, 61, 2403-2413.	7.9	32
108	<title>Development of microtomography imaging system for rock and mineral samples</title> . , 1999, 3772, 214.		31

#	Article	IF	CITATIONS
109	Fabrication of porous aluminum with deep pores by using Al–In monotectic solidification and electrochemical etching. Materials Letters, 2004, 58, 911-915.	2.6	31
110	Grain boundary tracking: A four-dimensional visualization technique for determining grain boundary geometry via local strain mapping. Acta Materialia, 2013, 61, 5535-5548.	7.9	31
111	<i>In Vivo</i> X-Ray Imaging Reveals Improved Airway Surface Hydration after a Therapy Designed for Cystic Fibrosis. American Journal of Respiratory and Critical Care Medicine, 2014, 190, 469-472.	5.6	31
112	Investigation of 3D Grain Shape Characteristics of Lunar Soil Retrieved in Apollo 16 Using Image-Based Discrete-Element Modeling. Journal of Aerospace Engineering, 2015, 28, .	1.4	31
113	Development of an X-ray imaging detector to resolve 200  nm line-and-space patterns by using transparent ceramics layers bonded by solid-state diffusion. Optics Letters, 2019, 44, 1403.	3.3	31
114	Refraction-enhanced tomography of mouse and rabbit lungs. Medical Physics, 2005, 32, 2787-2792.	3.0	30
115	In-situ High-resolution X-ray CT Observation of Compressive and Damage Behaviour of Aluminium Foams by Local Tomography Technique. Advanced Engineering Materials, 2006, 8, 473-475.	3.5	30
116	Phase contrast X-ray imaging for the non-invasive detection of airway surfaces and lumen characteristics in mouse models of airway disease. European Journal of Radiology, 2008, 68, S22-S26.	2.6	30
117	X-Ray Microtomographic Imaging of Three-Dimensional Structure of Soft Tissues. Tissue Engineering - Part C: Methods, 2008, 14, 359-363.	2.1	30
118	Threeâ€dimensional structures and elemental distributions of Stardust impact tracks using synchrotron microtomography and Xâ€ray fluorescence analysis. Meteoritics and Planetary Science, 2009, 44, 1203-1224.	1.6	30
119	Three-dimensional network of Drosophila brain hemisphere. Journal of Structural Biology, 2013, 184, 271-279.	2.8	30
120	Impact of melt convection induced by ultrasonic wave on dendrite growth in Sn–Bi alloys. Materials Letters, 2015, 150, 135-138.	2.6	30
121	Microstructural evolution of electrodes in sintering of multi-layer ceramic capacitors (MLCC) observed by synchrotron X-ray nano-CT. Acta Materialia, 2021, 206, 116605.	7.9	30
122	Four-Dimensional Annihilation Behaviors of Micro Pores during Surface Cold Working. Materials Transactions, 2010, 51, 1288-1295.	1.2	29
123	Diffraction-amalgamated grain boundary tracking for mapping 3D crystallographic orientation and strain fields during plastic deformation. Acta Materialia, 2016, 107, 310-324.	7.9	29
124	Influence of Mg on Solidification of Hypereutectic Cast Iron: X-ray Radiography Study. Metallurgical and Materials Transactions A: Physical Metallurgy and Materials Science, 2015, 46, 4937-4946.	2.2	28
125	Divergent evolution of medusozoan symmetric patterns: Evidence from the microanatomy of Cambrian tetramerous cubozoans from South China. Condwana Research, 2016, 31, 150-163.	6.0	28
126	Three-dimensional alteration of neurites in schizophrenia. Translational Psychiatry, 2019, 9, 85.	4.8	28

#	Article	IF	CITATIONS
127	Detecting micrometerâ€scale platinumâ€group minerals in mantle peridotite with microbeam synchrotron radiation Xâ€ray fluorescence analysis. Geochemistry, Geophysics, Geosystems, 2008, 9, .	2.5	27
128	Confocal full-field X-ray microscope for novel three-dimensional X-ray imaging. Journal of Synchrotron Radiation, 2009, 16, 616-621.	2.4	27
129	Investigation of internal structure of fine granules by microtomography using synchrotron X-ray radiation. International Journal of Pharmaceutics, 2013, 445, 93-98.	5.2	27
130	Numerical simulation of airflow and microparticle deposition in a synchrotron micro-CT-based pulmonary acinus model. Computer Methods in Biomechanics and Biomedical Engineering, 2015, 18, 1427-1435.	1.6	27
131	Nanomorphology of Itokawa regolith particles: Application to space-weathering processes affecting the Itokawa asteroid. Geochimica Et Cosmochimica Acta, 2016, 187, 195-217.	3.9	27
132	3D multiscale-imaging of processing-induced defects formed during sintering of hierarchical powder packings. Scientific Reports, 2019, 9, 11595.	3.3	27
133	3-D Image-Based Mechanical Simulation of Aluminium Foams: Effects of Internal Microstructure. Advanced Engineering Materials, 2006, 8, 459-467.	3.5	26
134	Development of an X-ray real-time stereo imaging technique using synchrotron radiation. Journal of Synchrotron Radiation, 2011, 18, 569-574.	2.4	26
135	Experimental constraints on permeable gas transport in crystalline silicic magmas. Contributions To Mineralogy and Petrology, 2012, 164, 493-504.	3.1	26
136	Development of vertically aligned ZnO-nanowires scintillators for high spatial resolution x-ray imaging. Applied Physics Letters, 2015, 106, .	3.3	26
137	Nondestructive Multiscale X-Ray Tomography by Combining Microtomography and High-Energy Phase-Contrast Nanotomography. Microscopy and Microanalysis, 2018, 24, 108-109.	0.4	26
138	Development of fast (sub-minute) micro-tomography. AIP Conference Proceedings, 2010, , .	0.4	25
139	In-situobservation of peritectic solidification in Sn-Cd and Fe-C alloys. IOP Conference Series: Materials Science and Engineering, 2012, 27, 012084.	0.6	25
140	High-resolution Observation of Steel Using X-ray Tomography Technique. ISIJ International, 2012, 52, 516-521.	1.4	25
141	High-pressure rotational deformation apparatus to 135 GPa. Review of Scientific Instruments, 2017, 88, 044501.	1.3	25
142	Impacts of Diabetes and an SGLT2 Inhibitor on the Glomerular Number and Volume in db/db Mice, as Estimated by Synchrotron Radiation Micro-CT at SPring-8. EBioMedicine, 2018, 36, 329-346.	6.1	25
143	High-energy x-ray nanotomography introducing an apodization Fresnel zone plate objective lens. Review of Scientific Instruments, 2021, 92, 023701.	1.3	25
144	Structural Analysis of Filler in Rubber Composite under Stretch with Time-Resolved Two-Dimensional Ultra-Small-Angle X-Ray Scattering. Rubber Chemistry and Technology, 2008, 81, 541-551.	1.2	24

#	Article	IF	CITATIONS
145	Influences of Hydrogen Micropores and Intermetallic Particles on Fracture Behaviors of Al-Zn-Mg-Cu Aluminum Alloys. Metallurgical and Materials Transactions A: Physical Metallurgy and Materials Science, 2016, 47, 6077-6089.	2.2	24
146	Quantitative and dynamic measurements of biologicalÂfresh samples with X-ray phase contrastÂtomography. Journal of Synchrotron Radiation, 2014, 21, 1347-1357.	2.4	24
147	Fast tomography using quasi-monochromatic undulator radiation. Journal of Synchrotron Radiation, 2006, 13, 403-407.	2.4	23
148	Analysis of inner structure in high-strength biodegradable fibers by X-ray microtomography using synchrotron radiation. Polymer, 2007, 48, 6145-6151.	3.8	23
149	Non-destructive observation of meteorite chips using quantitative analysis of optimized X-ray micro-computed tomography. Earth and Planetary Science Letters, 2010, 299, 359-367.	4.4	23
150	Effects of Hydrogen Micro Pores on Mechanical Properties in A2024 Aluminum Alloys. Materials Transactions, 2013, 54, 2195-2201.	1.2	23
151	Solidification of Sn-0.7Cu-0.15Zn Solder: In Situ Observation. Metallurgical and Materials Transactions A: Physical Metallurgy and Materials Science, 2014, 45, 918-926.	2.2	23
152	Optical properties of the lens: An explanation for the zones of discontinuity. Experimental Eye Research, 2014, 124, 93-99.	2.6	23
153	Optimizing lung aeration at birth using a sustained inflation and positive pressure ventilation in preterm rabbits. Pediatric Research, 2016, 80, 85-91.	2.3	23
154	Hydrogen partitioning behavior and related hydrogen embrittlement in Al-Zn-Mg alloys. Engineering Fracture Mechanics, 2019, 216, 106503.	4.3	23
155	Changes in Positive End-Expiratory Pressure Alter the Distribution of Ventilation within the Lung Immediately after Birth in Newborn Rabbits. PLoS ONE, 2014, 9, e93391.	2.5	23
156	Experimental reproduction of classic barred olivine chondrules: open-system behavior of chondrule formation. Geochimica Et Cosmochimica Acta, 2004, 68, 653-672.	3.9	22
157	Three-dimensional observation of the entangled eutectic structure in the Al2O3–YAG system. Journal of the European Ceramic Society, 2005, 25, 1397-1403.	5.7	22
158	Three-dimensional microtomographic imaging of human brain cortex. Brain Research, 2008, 1199, 53-61.	2.2	22
159	Characterization of a Hard X-ray Telescope at Synchrotron Facility SPring-8. Japanese Journal of Applied Physics, 2008, 47, 5743.	1.5	22
160	Application of Dual-Energy K-Edge Subtraction Imaging to Assessment of Heat Treatments in Al-Cu Alloys. Materials Transactions, 2010, 51, 2045-2048.	1.2	22
161	Spatial resolution of synchrotron x-ray microtomography in high energy range: Effect of x-ray energy and sample-to-detector distance. Applied Physics Letters, 2012, 101, .	3.3	22
162	Formation behaviour of blister in cast aluminium alloy. International Journal of Cast Metals Research, 2014, 27, 369-377.	1.0	22

#	Article	IF	CITATIONS
163	SPring-8 BL36XU: Catalytic Reaction Dynamics for Fuel Cells. Journal of Physics: Conference Series, 2016, 712, 012142.	0.4	22
164	Significant contribution of subseafloor microparticles to the global manganese budget. Nature Communications, 2019, 10, 400.	12.8	22
165	Methods for dynamic synchrotron X-ray respiratory imaging in live animals. Journal of Synchrotron Radiation, 2020, 27, 164-175.	2.4	22
166	A large-area CMOS imager as an X-ray detector for synchrotron radiation experiments. Journal of Synchrotron Radiation, 2004, 11, 347-352.	2.4	21
167	Localized morphometric deformations of small airways and alveoli in intact mouse lungs under quasi-static inflation. Respiratory Physiology and Neurobiology, 2005, 147, 51-63.	1.6	21
168	Seed-Dependent Deposition Behavior of AÎ <sup>2</sup> Peptides Studied with Wireless Quartz-Crystal-Microbalance Biosensor. Analytical Chemistry, 2011, 83, 4982-4988.	6.5	21
169	Three-dimensional evaluation of the compression and recovery behavior in a flexible graphite sheet by synchrotron radiation microtomography. Materials Characterization, 2012, 69, 52-62.	4.4	21
170	Measuring Airway Surface Liquid Depth in Ex Vivo Mouse Airways by X-Ray Imaging for the Assessment of Cystic Fibrosis Airway Therapies. PLoS ONE, 2013, 8, e55822.	2.5	21
171	X-ray phase-contrast computed tomography visualizes the microstructure and degradation profile of implanted biodegradable scaffolds after spinal cord injury. Journal of Synchrotron Radiation, 2015, 22, 136-142.	2.4	21
172	Influence of intermetallic particles on the initiation and growth behavior of hydrogen micropores during high-temperature exposure in Al-Zn-Mg-Cu aluminum alloys. Scripta Materialia, 2017, 135, 19-23.	5.2	21
173	Small airway changes in healthy and ovalbumin-treated mice during quasi-static lung inflation. Respiratory Physiology and Neurobiology, 2007, 156, 304-311.	1.6	20
174	Element-specific microtomographic imaging of <i>Drosophila</i> brain stained with high- <i>Z</i> probes. Journal of Synchrotron Radiation, 2008, 15, 374-377.	2.4	20
175	Dose distribution of a 125 keV mean energy microplanar x-ray beam for basic studies on microbeam radiotherapy. Medical Physics, 2008, 35, 3252-3258.	3.0	20
176	Three-dimensional observation of carbonaceous chondrites by synchrotron radiation X-ray CT – Quantitative analysis and developments for the future sample return missions. Geochimica Et Cosmochimica Acta, 2013, 116, 17-32.	3.9	20
177	Morphology of Nonmetallic-inclusion Clusters Observed in Molten Metal by X-ray Micro-Computed Tomography (CT). ISIJ International, 2013, 53, 1943-1952.	1.4	20
178	Three-dimensional imaging of plant tissues using X-ray micro-computed tomography. Plant Morphology, 2015, 27, 21-26.	0.1	20
179	A <i>Cloudina</i> -like fossil with evidence of asexual reproduction from the lowest Cambrian, South China. Geological Magazine, 2017, 154, 1294-1305.	1.5	20
180	New approaches to fabrication of multilayer Fresnel zone plate for high-energy synchrotron radiation X-rays. Vacuum, 2006, 80, 823-827.	3.5	19

#	Article	IF	CITATIONS
181	Measurement of electron density in dualâ€energy xâ€ray CT with monochromatic x rays and evaluation of its accuracy. Medical Physics, 2008, 35, 4924-4932.	3.0	19
182	Micro-CT observations of the 3D distribution of calcium oxalate crystals in cotyledons during maturation and germination inLotus miyakojimaeseeds. Microscopy (Oxford, England), 2013, 62, 353-361.	1.5	19
183	Sound velocity and elastic properties of Fe–Ni and Fe–Ni–C liquids at high pressure. Physics and Chemistry of Minerals, 2016, 43, 229-236.	0.8	19
184	Biphasic change and disuse-mediated regression of canal network structure in cortical bone of growing rats. Bone, 2007, 41, 239-246.	2.9	18
185	Development of x-ray laminography under an x-ray microscopic condition. Review of Scientific Instruments, 2011, 82, 073706.	1.3	18
186	SIZE AND DENSITY ESTIMATION FROM IMPACT TRACK MORPHOLOGY IN SILICA AEROGEL: APPLICATION TO DUST FROM COMET 81P/WILD 2. Astrophysical Journal, 2012, 744, 18.	4.5	18
187	Origin of ecdysis: fossil evidence from 535-million-year-old scalidophoran worms. Proceedings of the Royal Society B: Biological Sciences, 2019, 286, 20190791.	2.6	18
188	Defect Structure and Photovoltaic Characteristics of Internally Stacked CuO/Cu <sub>2</sub> O Photoactive Layer Prepared by Electrodeposition and Heating. ACS Applied Energy Materials, 2019, 2, 4833-4840.	5.1	18
189	Unification of analyser-based and propagation-based X-ray phase-contrast imaging. Nuclear Instruments and Methods in Physics Research, Section A: Accelerators, Spectrometers, Detectors and Associated Equipment, 2005, 548, 163-168.	1.6	17
190	Real-time non-invasive detection of inhalable particulates delivered into live mouse airways. Journal of Synchrotron Radiation, 2009, 16, 553-561.	2.4	17
191	In Situ Observation of Deformation in Semi-solid Fe-C Alloys at High Shear Rate. Metallurgical and Materials Transactions A: Physical Metallurgy and Materials Science, 2014, 45, 5613-5623.	2.2	17
192	Anatomy and affinities of a new 535â€millionâ€yearâ€old medusozoan from the Kuanchuanpu Formation, South China. Palaeontology, 2017, 60, 853-867.	2.2	17
193	Reconstruction of the multielement apparatus of the earliest Triassic conodont, <i>Hindeodus parvus</i> , using synchrotron radiation X-ray micro-tomography. Journal of Paleontology, 2017, 91, 1220-1227.	0.8	17
194	Influence of petrographic textures on the shapes of impact experiment fine fragments measuring several tens of microns: Comparison with Itokawa regolith particles. Icarus, 2018, 302, 109-125.	2.5	17
195	Submicrometer tomographic resolution examined using a micro-fabricated test object. Micron, 2010, 41, 90-95.	2.2	16
196	Structural mouthpart interaction evolved already in the earliest lineages of insects. Proceedings of the Royal Society B: Biological Sciences, 2015, 282, 20151033.	2.6	16
197	3D Fracture Behaviours in Dual-phase Stainless Steel. ISIJ International, 2016, 56, 883-892.	1.4	16
198	Method for estimating modulation transfer function from sample images. Micron, 2018, 105, 64-69.	2.2	16

#	Article	IF	CITATIONS
199	Discovery of primitive CO <sub>2</sub> -bearing fluid in an aqueously altered carbonaceous chondrite. Science Advances, 2021, 7, .	10.3	16
200	The universal sample holders of microanalytical instruments of FIB, TEM, NanoSIMS, and STXM-NEXAFS for the coordinated analysis of extraterrestrial materials. Earth, Planets and Space, 2020, 72, .	2.5	16
201	Simultaneous acquisition of dual analyser-based phase contrast X-ray images for small animal imaging. European Journal of Radiology, 2008, 68, S49-S53.	2.6	15
202	Estimation of presampling modulation transfer function in synchrotron radiation microtomography. Nuclear Instruments and Methods in Physics Research, Section A: Accelerators, Spectrometers, Detectors and Associated Equipment, 2010, 621, 615-619.	1.6	15
203	Stereological Analysis of Nonspherical Particles in Solid Metal. Metallurgical and Materials Transactions B: Process Metallurgy and Materials Processing Science, 2013, 44, 750-761.	2.1	15
204	Compression and recovery micro-mechanisms in flexible graphite. Carbon, 2013, 59, 184-191.	10.3	15
205	In Situ Observation of Void Nucleation and Growth in a Steel using X-ray Tomography. ISIJ International, 2015, 55, 1474-1482.	1.4	15
206	Three-dimensional X-ray visualization of axonal tracts in mouse brain hemisphere. Scientific Reports, 2016, 6, 35061.	3.3	15
207	Local Deformation and Fracture Behavior of High-Strength Aluminum Alloys Under Hydrogen Influence. Metallurgical and Materials Transactions A: Physical Metallurgy and Materials Science, 2020, 51, 1-19.	2.2	15
208	Optical development in the zebrafish eye lens. FASEB Journal, 2020, 34, 5552-5562.	0.5	15
209	Brain capillary structures of schizophrenia cases and controls show a correlation with their neuron structures. Scientific Reports, 2021, 11, 11768.	3.3	15
210	Measurement of hard X-ray coherence in the presence of a rotating random-phase-screen diffuser. Optics Communications, 2010, 283, 216-225.	2.1	14
211	Synchrotron Micro-XRF Measurements of Trace Element Distributions in BGA Type Solders and Solder Joints. Transactions of the Japan Institute of Electronics Packaging, 2010, 3, 40-46.	0.4	14
212	Threeâ€dimensional shapes and Fe contents of Stardust impact tracks: A track formation model and estimation of comet Wild 2 coma dust particle densities. Meteoritics and Planetary Science, 2010, 45, 1302-1319.	1.6	14
213	Development of high pressure apparatus for X-ray microtomography at SPring-8. Journal of Physics: Conference Series, 2010, 215, 012026.	0.4	14
214	Development of an X-ray Micro-Laminography System at SPring-8. , 2011, , .		14
215	Three-dimensional observation and morphological analysis of organic nanoglobules in a carbonaceous chondrite using X-ray micro-tomography. Geochimica Et Cosmochimica Acta, 2013, 116, 84-95.	3.9	14
216	Sagittal focusing of synchrotron radiation X-rays using a winged crystal. Journal of Synchrotron Radiation, 2013, 20, 219-225.	2.4	14

#	Article	IF	CITATIONS
217	Three-dimensional phase-contrast X-ray microtomographyÂwith scanning–imaging X-rayÂmicroscope optics. Journal of Synchrotron Radiation, 2013, 20, 793-800.	2.4	14
218	Detection of small internal fatigue cracks in Ti-6Al-4V by using synchrotron radiation μCT imaging. Mechanical Engineering Letters, 2016, 2, 16-00233-16-00233.	0.6	14
219	4D x-ray phase contrast tomography for repeatable motion of biological samples. Review of Scientific Instruments, 2016, 87, 093705.	1.3	14
220	Euendoliths versus ambient inclusion trails from Early Cambrian Kuanchuanpu Formation, South China. Palaeogeography, Palaeoclimatology, Palaeoecology, 2017, 476, 147-157.	2.3	14
221	Fresnel zone plate with apodized aperture for hard X-ray Gaussian beam optics. Journal of Synchrotron Radiation, 2017, 24, 586-594.	2.4	14
222	Metasomatic PGE mobilization by carbonatitic melt in the mantle: Evidence from sub-μm-scale sulfide–carbonaceous glass inclusion in Tahitian harzburgite xenolith. Chemical Geology, 2017, 475, 87-104.	3.3	14
223	Short crack growth behavior and its transitional interaction with 3D microstructure in Ti-6Al-4V. Materials Science & Engineering A: Structural Materials: Properties, Microstructure and Processing, 2018, 738, 229-237.	5.6	14
224	Forearm bone histology of the small theropod <i>Daliansaurus liaoningensis</i> (Paraves:) Tj ETQq0 0 0 rgBT /C	)verlock 10 1:4	) Tf <sub>1</sub> 50 462 Td
225	Bone tissue histology of the Early Cretaceous bird <i>Yanornis</i> : evidence for a diphyletic origin of modern avian growth strategies within Ornithuromorpha. Historical Biology, 2020, 32, 1422-1434.	1.4	14
226	Three-dimensional structural measurement and material identification of an all-solid-state lithium-ion battery by X-Ray nanotomography and deep learning. Journal of Power Sources Advances, 2021, 8, 100048.	5.1	14
227	Damage micromechanisms in high Mn and Zn content 7XXX aluminum alloys. Materials Science & Engineering A: Structural Materials: Properties, Microstructure and Processing, 2020, 793, 139423.	5.6	14
228	Evaluation of the improved three-dimensional resolution of a synchrotron radiation computed tomograph using a micro-fabricated test pattern. Journal of Synchrotron Radiation, 2008, 15, 648-654.	2.4	13
229	Local crack driving force analysis of a fatigue crack by a microstructural tracking method. Scripta Materialia, 2009, 61, 489-492.	5.2	13
230	Chain structure in the unidirectionally solidified Al2O3–YAG–ZrO2 eutectic composite. Journal of Crystal Growth, 2009, 311, 3765-3770.	1.5	13
231	Quasi-kinoform type multilayer zone plate with high diffraction efficiency for high-energy X-rays. Journal of Physics: Conference Series, 2009, 186, 012075.	0.4	13
232	Present Status of the Nanotomography System at BL47XU at SPring-8 and Its Efficiency Improvement Using Double-Condenser Optics. AIP Conference Proceedings, 2011, , .	0.4	13
233	Three-Dimensional Cortical Bone Microstructure in a Rat Model of Hypoxia-Induced Growth Retardation. Calcified Tissue International, 2011, 88, 54-62.	3.1	13
234	X-ray Computerized Tomography Observation of the Interfacial Structure of Liquid Marbles. Bulletin of the Chemical Society of Japan, 2015, 88, 84-88.	3.2	13

#	Article	IF	CITATIONS
235	Three-Dimensional Neuronal Structure of Human Cerebral Cortex Determined by Synchrotron-Radiation Microtomography. Microscopy and Microanalysis, 2015, 21, 919-920.	0.4	13
236	Three-dimensional Observation of Nonmetallic Inclusion Clusters in Solid Metal by X-ray Micro-CT. ISIJ International, 2016, 56, 1989-1995.	1.4	13
237	Time-resolved X-ray imaging of solidification cracking for Al-Cu alloy at the weld crater. Materials Characterization, 2020, 167, 110469.	4.4	13
238	Electrical Conductivity in Texturally Equilibrated Fluidâ€Bearing Forsterite Aggregates at 800°C and 1ÂGPa: Implications for the High Electrical Conductivity Anomalies in Mantle Wedges. Journal of Geophysical Research: Solid Earth, 2021, 126, e2020JB021343.	3.4	13
239	High-sensitive imaging with scanning transmission hard X-ray microscope. European Physical Journal Special Topics, 2003, 104, 41-44.	0.2	13
240	High-definition high-throughput micro-tomography at SPring-8. Journal of Physics: Conference Series, 2009, 186, 012050.	0.4	12
241	A new technique to examine individual pollutant particle and fibre deposition and transit behaviour in live mouse trachea. Journal of Synchrotron Radiation, 2010, 17, 719-729.	2.4	12
242	Assessment of the use of a diffuser in propagation-based x-ray phase contrast imaging. Optics Express, 2010, 18, 13478.	3.4	12
243	Particle Coagulation in Molten Metal Based on Three-Dimensional Analysis of Cluster by X-Ray Micro-Computer Tomography (CT). ISIJ International, 2013, 53, 1958-1967.	1.4	12
244	Rheological transitions in highâ€ŧemperature volcanic fault zones. Journal of Geophysical Research: Solid Earth, 2015, 120, 2974-2987.	3.4	12
245	Quantitative tomography of hydrogen precharged and uncharged Al-Zn-Mg-Cu alloy after tensile fracture. Materials Science & Engineering A: Structural Materials: Properties, Microstructure and Processing, 2016, 670, 300-313.	5.6	12
246	Investigation of three-dimensional morphology changes of the eutectic Si particles affected by trace P and Sr in Al-7%Si cast alloys by means of synchrotron nano-tomography. Materials Characterization, 2017, 130, 237-242.	4.4	12
247	Observation of Morphology Changes of Fine Eutectic Si Phase in Al-10%Si Cast Alloy during Heat Treatment by Synchrotron Radiation Nanotomography. Materials, 2018, 11, 1308.	2.9	12
248	A Modeling Approach for Investigating Opto-Mechanical Relationships in the Human Eye Lens. IEEE Transactions on Biomedical Engineering, 2020, 67, 999-1006.	4.2	12
249	In situ observation of solidification crack propagation for type 310S and 316L stainless steels during TIG welding using synchrotron X-ray imaging. Journal of Materials Science, 2021, 56, 10653-10663.	3.7	12
250	Photon-counting, energy-resolving and super-resolution phase contrast X-ray imaging using an integrating detector Optics Express, 2020, 28, 7080.	3.4	12
251	Hard X-Ray Microtomography Using X-Ray Imaging Optics. Japanese Journal of Applied Physics, 2001, 40, 1499-1503.	1.5	11
252	The effects of microstructure on creep behaviour—A study through synchrotron X-ray tomography. Materials Science & Engineering A: Structural Materials: Properties, Microstructure and Processing, 2009, 513-514, 222-227.	5.6	11

#	Article	IF	CITATIONS
253	Airway distension during lung inflation in healthy and allergic-sensitised mice in vivo. Respiratory Physiology and Neurobiology, 2013, 185, 639-646.	1.6	11
254	Multilevel-type multilayer X-ray lens (Fresnel zone plate) by sputter deposition. Vacuum, 2008, 83, 691-694.	3.5	10
255	High-resolution visualization of tumours in rabbit lung using refraction contrast X-ray imaging. European Journal of Radiology, 2008, 68, S54-S57.	2.6	10
256	Microstructural Quantification of Granular Assembly studied by Micro X-ray CT at SPring-8. Journal of Applied Mechanics, 2008, 11, 507-515.	0.1	10
257	Investigation of Imaging Properties of Mouse Eyes Using X-ray Phase Contrast Tomography. AIP Conference Proceedings, 2010, , .	0.4	10
258	Micro-pore development phenomenon in hydrogen pre-charged aluminum alloy studied using synchrotron X-ray micro-tomography. Applied Physics Letters, 2013, 103, 1098/Math/MathML	3.3	10
259	altimg="si0006.gif" overflow="scroll"> <mml:mi mathvariant="normal"&gt;A<mml:msub><mml:mrow><mml:mi>î<sup>2</sup></mml:mi></mml:mrow>&lt; peptide on ultrasonically formed <mml:math <br="" xmlns:mml="http://www.w3.org/1998/Math/MathML">altimg="si0007.gif" overflow="scroll"&gt;<mml:mi< td=""><td><mml:mn> 10.1</mml:mn></td><td>1 10</td></mml:mi<></mml:math></mml:msub></mml:mi 	<mml:mn> 10.1</mml:mn>	1 10
260	mathvariant="normal">Ac/mmhmi> conmhmsub> conmhmrow> conmhmi>î² c/mm. Biosensors and Mechanisms of Ultrasonically Induced Fibrillation of Amyloid β < sub>1–40 < /sub> Peptides. Japanese Journal of Applied Physics, 2013, 52, 07HE10.	1.5	10
261	Recent progress of hard x-ray imaging microscopy and microtomography at BL37XU of SPring-8. AIP Conference Proceedings, 2016, , .	0.4	10
262	Advancement of magma fragmentation by inhomogeneous bubble distribution. Scientific Reports, 2017, 7, 16755.	3.3	10
263	Initiation and propagation of small fatigue crack in beta titanium alloy observed through synchrotron radiation multiscale computed tomography. Engineering Fracture Mechanics, 2022, 263, 108308.	4.3	10
264	Distribution of electron density using dual-energy X-ray CT. IEEE Transactions on Nuclear Science, 2003, 50, 1678-1682.	2.0	9
265	Direct Measurement of the Resolving Power of X-ray CT System in SPring-8. AIP Conference Proceedings, 2004, , .	0.4	9
266	X-ray imaging microscopy using Fresnel zone plate objective and quasimonochromatic undulator radiation. Review of Scientific Instruments, 2004, 75, 1155-1157.	1.3	9
267	Wavelet-based local region-of-interest reconstruction for synchrotron radiation x-ray microtomography. Journal of Applied Physics, 2007, 102, 114908.	2.5	9
268	Assessment of 3D inhomogeneous microstructure of highly alloyed aluminium foam via dual energy K-edge subtraction imaging. Philosophical Magazine, 2010, 90, 1853-1871.	1.6	9
269	Synchrotron radiography of direct-shear in semi-solid alloys. IOP Conference Series: Materials Science and Engineering, 2012, 27, 012086.	0.6	9
270	Hard X-ray Imaging Microscopy using X-ray Guide Tube as Beam Condenser for Field Illumination. Journal of Physics: Conference Series, 2013, 463, 012028.	0.4	9

#	Article	IF	CITATIONS
271	Ideal Osmotic Spaces for Chlorobionts or Cyanobionts Are Differentially Realized by Lichenized Fungi Â Â. Plant Physiology, 2014, 166, 337-348.	4.8	9
272	Note: High-pressure in situ x-ray laminography using diamond anvil cell. Review of Scientific Instruments, 2016, 87, 046105.	1.3	9
273	Combined FIB microsampling and X-ray microtomography: a powerful tool for the study of tiny fluid inclusions. European Journal of Mineralogy, 2016, 28, 245-256.	1.3	9
274	Introducing high efficiency image detector to X-ray imaging tomography. Journal of Physics: Conference Series, 2017, 849, 012051.	0.4	9
275	An intermediate type of medusa from the early Cambrian Kuanchuanpu Formation, South China. Palaeontology, 2020, 63, 775-789.	2.2	9
276	Fracture behavior of thermally aged Ag–Cu composite sinter joint through microscale tensile test coupled with nano X-ray computed tomography. Materials and Design, 2021, 206, 109818.	7.0	9
277	Three-dimensional observation of micro-pores in a 2024 aluminum alloy by synchrotron X-ray projection- and imaging-type microtomography techniques. Keikinzoku/Journal of Japan Institute of Light Metals, 2009, 59, 30-34.	0.4	8
278	Performance Test and Evaluation of Multilevel Fresnel Zone Plate with Three-Step Profile Fabricated with Electron-Beam Lithography. Japanese Journal of Applied Physics, 2012, 51, 022502.	1.5	8
279	Visualization of nanoscale deformation in polymer composites with zernike-type phase-contrast X-ray microscopy and the finite element method. Polymer Journal, 2013, 45, 64-69.	2.7	8
280	Structural changes of polymer-coated microgranules and excipients on tableting investigated by microtomography using synchrotron X-ray radiation. International Journal of Pharmaceutics, 2015, 481, 132-139.	5.2	8
281	Refractive index degeneration in older lenses: A potential functional correlate to structural changes that underlie cataract formation. Experimental Eye Research, 2015, 140, 19-27.	2.6	8
282	State of 3-D micro-damage in hydrogen redistributed regions of precharged high strength aluminium alloy. Corrosion Science, 2016, 111, 26-38.	6.6	8
283	Electrochemically Grown ZnO Vertical Nanowire Scintillator with Lightâ€Guiding Effect. Physica Status Solidi (A) Applications and Materials Science, 2017, 214, 1700285.	1.8	8
284	Synchrotron X-ray diffraction characterization of the inheritance of GaN homoepitaxial thin films grown on selective growth substrates. CrystEngComm, 2018, 20, 2861-2867.	2.6	8
285	Anvil design for slip-free high pressure deformation experiments in a rotational diamond anvil cell. High Pressure Research, 2018, 38, 23-31.	1.2	8
286	Effects of 3D microstructural distribution on short crack growth behavior in two bimodal Ti–6Al–4V alloys. Materials Science & Engineering A: Structural Materials: Properties, Microstructure and Processing, 2019, 766, 138264.	5.6	8
287	Development of a sample holder for synchrotron radiation-based computed tomography and diffraction analysis of extraterrestrial materials. Review of Scientific Instruments, 2020, 91, 035107.	1.3	8
288	Oxysterol Compounds in Mouse Mutant αA- and αB-Crystallin Lenses Can Improve the Optical Properties		8

of the Lens. , 2022, 63, 15.

#	Article	IF	CITATIONS
289	Detection of small internal fatigue cracks in Tiâ€6Alâ€4V via synchrotron radiation nanocomputed tomography. Fatigue and Fracture of Engineering Materials and Structures, 2022, 45, 2693-2702.	3.4	8
290	A Study of Three-dimensional Structures of Rocks and Minerals Using a High-resolution X-ray CT Method. Journal of Geography (Chigaku Zasshi), 2000, 109, 845-858.	0.3	7
291	Observations of three-dimensional microstructures of symplectite minerals in the Horoman Peridotite Complex using a high-resolution X-ray CT system at Spring-8. Journal of the Geological Society of Japan, 2003, 109, III-IV.	0.6	7
292	Sarcoptes scabiei var. hominis: Three-dimensional structure of a female imago and crusted scabies lesions by X-ray micro-CT. Experimental Parasitology, 2009, 122, 268-272.	1.2	7
293	A high precision recipe for correcting images distorted by a tapered fiber optic. Journal of Instrumentation, 2010, 5, P09008-P09008.	1.2	7
294	Building Human Brain Network in 3D Coefficient Map Determined by X-ray Microtomography. AlP Conference Proceedings, 2011, , .	0.4	7
295	In Vivo CT Quantification of Trabecular Bone Dynamics in Mice after Sciatic Neurectomy Using Monochromatic Synchrotron Radiation. Calcified Tissue International, 2011, 88, 432-441.	3.1	7
296	Extracting tissue and cell outlines of Arabidopsis seeds using refraction contrast X-ray CT at the SPring-8 facility. AIP Conference Proceedings, 2012, , .	0.4	7
297	Optimization of X-ray phase contrast imaging system toward high-sensitivity measurements of biological organs. AIP Conference Proceedings, 2012, , .	0.4	7
298	Current status of ASTRO-H Hard X-ray Telescopes (HXTs). , 2012, , .		7
299	Development of large-field high-resolution hard x-ray imaging microscopy and microtomography with Fresnel zone plate objective. , 2013, , .		7
300	Imaging lung tissue oscillations using high-speed X-ray velocimetry. Journal of Synchrotron Radiation, 2016, 23, 324-330.	2.4	7
301	High-energy, high-resolution x-ray imaging for metallic cultural heritages. AIP Advances, 2017, 7, .	1.3	7
302	Assessment of predominant microstructural features controlling 3D short crack growth behavior via a surrogate approach in Ti-6Al-4V. Materials Science & Engineering A: Structural Materials: Properties, Microstructure and Processing, 2019, 751, 351-362.	5.6	7
303	An experimental system for time-resolved x-ray diffraction of deforming silicate melt at high temperature. Review of Scientific Instruments, 2020, 91, 095113.	1.3	7
304	Direct observations of nucleant TiB2 particles in cast aluminum by synchrotron radiation multiscale tomography. Materialia, 2020, 10, 100663.	2.7	7
305	Cell compaction is not required for the development of gradient refractive index profiles in the embryonic chick lens. Experimental Eye Research, 2020, 197, 108112.	2.6	7
306	Visualization of Arabidopsis root system architecture in 3D by refraction-contrast X-ray micro-computed tomography. Microscopy (Oxford, England), 2021, 70, 536-544.	1.5	7

#	Article	IF	CITATIONS
307	Mineralogy of fine-grained matrix, fine-grained rim, chondrule rim, and altered mesostasis of a chondrule in Asuka 12169, one of the least altered CM chondrites. Polar Science, 2021, 29, 100727.	1.2	7
308	Development of an X-ray imaging detector for high-energy X-ray microtomography. Journal of Synchrotron Radiation, 2020, 27, 934-940.	2.4	7
309	Emphysema quantified: mapping regional airway dimensions using 2D phase contrast X-ray imaging. Biomedical Optics Express, 2020, 11, 4176.	2.9	7
310	Double-multilayer monochromators for high-energy and large-field X-ray imaging applications with intense pink beams at SPring-8 BL20B2. Journal of Synchrotron Radiation, 2022, 29, 1265-1272.	2.4	7
311	Morphometric Deformations of Small Airways and Alveoli under Quasi-static Inflation Process. Journal of Physiological Anthropology and Applied Human Science, 2005, 24, 465-468.	0.4	6
312	Three-dimensional observation of ductile fracture process by deflection contrast imaging in cast Al–7%Si alloys. Keikinzoku/Journal of Japan Institute of Light Metals, 2008, 58, 58-64.	0.4	6
313	Hollow-Cone Illumination for Hard X-ray Imaging Microscopy by Rotating-Grating Condenser Optics. AIP Conference Proceedings, 2011, , .	0.4	6
314	Real Time Synchrotron X-Ray Imaging for Nucleation and Growth of Cu <sub>6</sub> Sn <sub>5</sub> in Sn-7Cu-0.05Ni High Temperature Lead-Free Solder Alloys. Advanced Materials Research, 2012, 626, 200-204.	0.3	6
315	Imaging and spectral performance of CdTe double-sided strip detectors for the hard x-ray imager onboard ASTRO-H. , 2012, , .		6
316	Development of X-ray triscopic imaging system towards three-dimensional measurements of dynamical samples. Journal of Instrumentation, 2013, 8, C05002-C05002.	1.2	6
317	Application of Diffraction-Amalgamated Grain Boundary Tracking to Fatigue Crack Propagation Behavior in High Strength Aluminum Alloy. Materials Transactions, 2015, 56, 424-428.	1.2	6
318	Analysis system of submicron particle tracks in the fine-grained nuclear emulsion by a combination of hard x-ray and optical microscopy. Review of Scientific Instruments, 2015, 86, 073701.	1.3	6
319	Evolution Behavior of Hydrogen-Induced Nano Voids in Al–Zn–Mg–Cu Aluminum Alloys under Loading. Materials Transactions, 2018, 59, 1532-1535.	1.2	6
320	The Role of Hydrogen on the Local Fracture Toughness Properties of 7XXX Aluminum Alloys. Metallurgical and Materials Transactions A: Physical Metallurgy and Materials Science, 2018, 49, 5368-5381.	2.2	6
321	The effects of possible contamination by sample holders on samples to be returned by Hayabusa2. Meteoritics and Planetary Science, 2020, 55, 1665-1680.	1.6	6
322	Structural diverseness of neurons between brain areas and between cases. Translational Psychiatry, 2021, 11, 49.	4.8	6
323	Contributions of shape and stiffness to accommodative loss in the ageing human lens: a finite element model assessment. Journal of the Optical Society of America A: Optics and Image Science, and Vision, 2019, 36, B116.	1.5	6
324	Change in microstructure of Al–Si–Cu casting alloys during high temperature solution treatment. International Journal of Cast Metals Research, 2008, 21, 114-118.	1.0	5

#	Article	IF	CITATIONS
325	Differential Phase-Contrast Scanning X-Ray Microscope For Observation Of Low-Z element Specimen. AIP Conference Proceedings, 2010, , .	0.4	5
326	X-ray microtomographic visualization of <i>EscherichiaÂcoli</i> by metalloprotein overexpression. Journal of Synchrotron Radiation, 2013, 20, 581-586.	2.4	5
327	ASTRO-H Hard X-ray Telescope (HXT). , 2014, , .		5
328	Performance of ASTRO-H hard x-ray telescope (HXT). , 2016, , .		5
329	Studies of print-through and reflectivity of x-ray mirrors using thin carbon-fiber-reinforced plastic. Journal of Astronomical Telescopes, Instruments, and Systems, 2016, 2, 014002.	1.8	5
330	Improvement of quantitative performance of imaging x-ray microscope by reduction of edge-enhancement effect. Journal of Physics: Conference Series, 2017, 849, 012055.	0.4	5
331	X-Ray Imaging of Formation and Growth of Spheroidal Graphite in Ductile Cast Iron. Materials Science Forum, 2018, 925, 104-109.	0.3	5
332	<title>X-ray imaging microscope with a partial coherent illumination</title> ., 2001, , .		5
333	Non-Destructive Measurement of Internal Small Fatigue Crack Growth Rate in Ti-6Al-4V. Zairyo/Journal of the Society of Materials Science, Japan, 2017, 66, 928-934.	0.2	5
334	Current Status of Microtomography with Synchrotron Radiation X-ray Source. Journal of the Vacuum Society of Japan, 2011, 54, 47-55.	0.3	5
335	Three-dimensional microstructure and mineralogy of a cosmic symplectite in the Acfer 094 carbonaceous chondrite: Implication for its origin. Geochimica Et Cosmochimica Acta, 2022, 323, 220-241.	3.9	5
336	Nondestructive Evaluation of Thermal Phase Growth in Solder Ball Micro-Joints by Synchrotron Radiation X-Ray Micro-Tomography. , 2005, , 1115.		4
337	Current status of hard x-ray characterization of ASTRO-H HXT at SPring-8. , 2010, , .		4
338	Fabrication and testing of sputtered-sliced kinoform style Fresnel zone plate. Vacuum, 2010, 84, 1457-1459.	3.5	4
339	Regular Structure Formation of Hypermonotectic Al-In Alloys. Materials Science Forum, 2010, 649, 131-136.	0.3	4
340	Angular resolution measurements at SPring-8 of a hard x-ray optic for the New Hard X-ray Mission. Proceedings of SPIE, 2011, , .	0.8	4
341	Localized deformation during fracture of high-strength aluminum alloy. Procedia Engineering, 2011, 10, 2591-2596.	1.2	4
342	Differential phase contrast x-ray microimaging with scanning-imaging x-ray microscope optics. Review of Scientific Instruments, 2012, 83, 083701.	1.3	4

#	Article	IF	CITATIONS
343	Recent results of hard x-ray characterization of ASTRO-H HXT at SPring-8. Proceedings of SPIE, 2012, , .	0.8	4
344	Large-Field X-ray Imaging at SPring-8 BL20B2. Synchrotron Radiation News, 2015, 28, 30-35.	0.8	4
345	Differential-phase-contrast knife-edge scan method for precise evaluation of X-ray nanobeam. Japanese Journal of Applied Physics, 2015, 54, 092401.	1.5	4
346	Spatiotemporal development of soaked protein crystal. Scientific Reports, 2014, 4, 5731.	3.3	4
347	Morphology of Nonmetallic-inclusion Clusters Observed in Molten Metal by X-ray Micro-CT. Tetsu-To-Hagane/Journal of the Iron and Steel Institute of Japan, 2015, 101, 148-157.	0.4	4
348	Three-Dimensional Investigation of Void Coalescence in Free-Cutting Steel using X-ray Tomography. ISIJ International, 2015, 55, 1483-1488.	1.4	4
349	In vivo monitoring of bone microstructure by propagation-based phase-contrast computed tomography using monochromatic synchrotron light. Laboratory Investigation, 2020, 100, 72-83.	3.7	4
350	Diffraction-Amalgamated Grain-boundary Tracking (DAGT) technique and its application to an aluminum alloy. , 2012, , 9-14.		4
351	Morphology of Palaeospondylus shows affinity to tetrapod ancestors. Nature, 2022, 606, 109-112.	27.8	4
352	Direct Three-Dimensional Observation of Phase Structures in a Non-aqueous Physical Gel by Synchrotron X-ray CT. Kobunshi Ronbunshu, 2003, 60, 373-376.	0.2	3
353	Facile Synthesis of <i>C</i> <sub>2</sub> -Symmetric Chiral Crown Ethers with Two Reactive Hydroxymethyl Groups. Synthesis, 2007, 2007, 2973-2978.	2.3	3
354	Quasi-blazed type multilayer zone plate for X-rays. Vacuum, 2009, 84, 578-580.	3.5	3
355	Observation of kinoform-style multilayer Fresnel zone plate by scanning ion microscopy. Vacuum, 2009, 84, 669-671.	3.5	3
356	Current status of the Astro-H X-ray Telescope system. , 2009, , .		3
357	Optimizing the Illumination in a Hard X-ray Microscope with Integrated Talbot Interferometer. AIP Conference Proceedings, 2011, , .	0.4	3
358	Combined Lung Imaging and Respiratory Physiology Research at SPring-8. Synchrotron Radiation News, 2011, 24, 19-23.	0.8	3
359	Single grating x-ray imaging for dynamic biological systems. , 2012, , .		3
360	Microstructure of Multilayer Fresnel Zone Plate for X-ray Focusing. Physics Procedia, 2012, 32, 157-160.	1.2	3

#	Article	IF	CITATIONS
361	Characterization of Cell Wall Microstructure and Damage Behavior of Alloyed Aluminum Foam via Synchrotronâ€Based Microtomography. Advanced Engineering Materials, 2013, 15, 149-152.	3.5	3
362	X-ray micro-tomography using white beam radiation from SPring-8. Journal of Instrumentation, 2013, 8, P07018-P07018.	1.2	3
363	Effects of Stress Triaxiality on Damage Evolution from Pre-Existing Hydrogen Pores in Aluminum Alloy. Materials Transactions, 2014, 55, 383-386.	1.2	3
364	Development of micro-tomography system for materials science at SPring-8. , 2016, , .		3
365	Use of ionic liquid for X-ray micro-CT specimen preparation of imbibed seeds. Microscopy (Oxford,) Tj ETQq1 1 (	).784314 1.5	rgBŢ /Overlac
366	The disuse effect on canal network structure and oxygen supply in the cortical bones of rats. Biomechanics and Modeling in Mechanobiology, 2019, 18, 375-385.	2.8	3
367	Localized Photoluminescence Imaging of Bi‣ayered Cuprous/Cupric Oxide Semiconductor Films by Synchrotron Radiation. Physica Status Solidi (B): Basic Research, 2019, 256, 1800119.	1.5	3
368	<i>In situ</i> Observation of Dendrite Growth in Sn-Bi Alloys under Ultrasonic Vibration Using Time-resolved X-ray Imaging. Tetsu-To-Hagane/Journal of the Iron and Steel Institute of Japan, 2016, 102, 170-178.	0.4	3
369	Novel application of sputtered-sliced concentric multilayers to various optical elements for synchrotron radiation high-brilliance X-ray beamlines at SPring-8. Vacuum, 2004, 74, 741-746.	3.5	2
370	3D Particle Characteristics of Highland Lunar Soil (No. 60501) Obtained by Micro X-Ray CT. , 2008, , .		2
371	Simultaneous Measurement of Oxygen Diffusivity and Visualization of Moisture Distribution in Gas Diffusion Layer with Wettability Distribution for Improvement of Polymer Electrolyte Fuel Cell Performance. 880-02 Nihon Kikai Gakkai Ronbunshū Transactions of the Japan Society of Mechanical Engineers Series B B-hen, 2011, 77, 2019-2027.	0.2	2
372	Three Dimensional and Nondestructive Evaluation of Thermal Fatigue Crack Propagation Process in Complex-Shaped Solder Joints by Synchrotron Radiation X-Ray Micro-Tomography. , 2011, , .		2
373	Nondestructive Three-Dimensional Observation of the Influence of Zirconium Inclusions in Laser-Irradiated Fusion-Spliced Optical Fiber on Core Structure Changes Using Synchrotron Radiation X-ray Micro-Computed Tomography. Japanese Journal of Applied Physics, 2013, 52, 096602.	1.5	2
374	Recent progress in the ground calibration of the ASTRO-H Hard X-ray telescope (HXT-2). , 2014, , .		2
375	Particle Coagulation in Molten Metal Based on Three-Dimensional Analysis of Cluster by X-Ray Micro-Computer Tomography (CT). Tetsu-To-Hagane/Journal of the Iron and Steel Institute of Japan, 2015, 101, 158-167.	0.4	2
376	Development of sealed sample containers and high resolution micro-tomography. AIP Conference Proceedings, 2016, , .	0.4	2
377	Three-dimensional structure of brain tissue at submicrometer resolution. AIP Conference Proceedings, 2016, , .	0.4	2
378	Rheology of basaltic ash from Stromboli volcano inferred from intermittent compression experiments. Journal of Volcanology and Geothermal Research, 2017, 343, 211-219.	2.1	2

#	Article	IF	CITATIONS
379	Observation of the initial process of internal fracture in very high cycle fatigue in Ti-6Al-4V by synchrotron radiation μCT imaging. Transactions of the JSME (in Japanese), 2017, 83, 17-00104-17-00104.	0.2	2
380	Effect of Cumulative Surface on Pore Development in Chalk. Water Resources Research, 2019, 55, 4801-4819.	4.2	2
381	Hydrogen desorption behavior in Al–8%Zn–1%Mg alloy. Keikinzoku/Journal of Japan Institute of Light Metals, 2019, 69, 186-193.	0.4	2
382	Sound velocity and density of liquid Ni68S32 under pressure using ultrasonic and X-ray absorption with tomography methods. Comptes Rendus - Geoscience, 2019, 351, 163-170.	1.2	2
383	Characterization of the Multicellular Membraneâ€Bearing Algae From the Kuanchuanpu Biota (Cambrian: Terreneuvian). Journal of Geophysical Research G: Biogeosciences, 2021, 126, e2020JG006102.	3.0	2
384	Development of the Pectoral Lobed Fin in the Australian Lungfish Neoceratodus forsteri. Frontiers in Ecology and Evolution, 2021, 9, .	2.2	2
385	Dichotomy in formation and growth of bones of Yanornis martini (Pygostylia, Ornithuromorpha): study of thermal regime in an extinct bird. Historical Biology, 0, , 1-24.	1.4	2
386	Turbulent Coagulation of Solid Particles in Molten Aluminium—Kinetics of Cluster Formation. , 2012, , 1337-1342.		2
387	W-Concentration 3D Mapping in SKH51 Steel by Dual-Energy K-Absorption Edge Subtraction Imaging. ISIJ International, 2014, 54, 141-147.	1.4	2
388	Development of high energy micro-tomography system at SPring-8. , 2017, , .		2
389	Internal structure changes of eyelash induced by eye makeup. Journal of Cosmetic Science, 2014, 65, 217-24.	0.1	2
390	Thermo-mechanical fatigue property of a surface-hardened AC4CH cast aluminum alloy. Keikinzoku/Journal of Japan Institute of Light Metals, 2008, 58, 236-241.	0.4	1
391	Growth behavior of hydrogen micro pores during ductile fracture of a 5154 aluminum alloy. Keikinzoku/Journal of Japan Institute of Light Metals, 2010, 60, 409-410.	0.4	1
392	SPring-8 X-Ray Micro-Tomography Observations of Zirconium Inclusions in CO\$_{2} Laser Fusion Splice for Single Mode Optical Fibers. IEEE Transactions on Components, Packaging and Manufacturing Technology, 2011, 1, 100-110.	2.5	1
393	3D/4D Strain Mapping Using <i>In Situ</i> X-Ray Microtomography. Applied Mechanics and Materials, 0, 70, 249-254.	0.2	1
394	Development of Scanning-Imaging X-Ray Microscope for Quantitative Three-Dimensional Phase Contrast Microimaging. Journal of Physics: Conference Series, 2013, 463, 012034.	0.4	1
395	First result from a ground calibration of the Hard X-ray Telescope (HXT) onboard ASTRO-H satellite. Proceedings of SPIE, 2013, , .	0.8	1
396	3D/4D fracture mechanics evaluation on shear band of aluminum alloys. Keikinzoku/Journal of Japan Institute of Light Metals, 2013, 63, 188-195.	0.4	1

#	Article	IF	CITATIONS
397	Relationship between resolution and rotation stage in imaging X-ray CT. Keikinzoku/Journal of Japan Institute of Light Metals, 2013, 63, 273-278.	0.4	1
398	Development of 3D Deformation Analysis Method in Polycrystalline Metal by Combining Synchrotron Radiation Tomography with X-Ray Diffraction. Nippon Kinzoku Gakkaishi/Journal of the Japan Institute of Metals, 2013, 77, 375-384.	0.4	1
399	Application of Synchrotron Radiation X-Ray Laminography to Nondestructive Evaluation of the Fatigue Crack Propagation Process in Flip Chip Solder Joints. , 2013, , .		1
400	Image-based finite element analysis for reverse 4D materials engineering: ductile fracture originated from hydrogen pores. Keikinzoku/Journal of Japan Institute of Light Metals, 2014, 64, 611-612.	0.4	1
401	C5-P-02Distribution of intercellular spaces in plant seeds during imbibition and germination observed using X-ray micro-CT. Microscopy (Oxford, England), 2015, 64, i139.2-i139.	1.5	1
402	C3-P-033-D cell geometrical analysis of epidermal and cortical cells in hypocotyl-root axes in arabidopsis seeds using X-ray micro-CT. Microscopy (Oxford, England), 2015, 64, i127.2-i127.	1.5	1
403	Localization of shear strain and shear band formation induced by deformation in semi-solid Al-Cu alloys. IOP Conference Series: Materials Science and Engineering, 2015, 84, 012078.	0.6	1
404	Progress of projection computed tomography by upgrading of the beamline 37XU of SPring-8. AIP Conference Proceedings, 2016, , .	0.4	1
405	In-Situ Monitoring via Synchrotron Radiation Laminography of Thermal Fatigue Cracks at Die-Attached Joints Under Cyclic Energization Loading. , 2017, , .		1
406	Current status of X-ray phase imaging at SPring-8: Toward 4D X-ray phase tomography for biological samples. Journal of Physics: Conference Series, 2017, 849, 012054.	0.4	1
407	Three-dimensional study by synchrotron radiation computed tomography of melt distribution in samples doped to enhance contrast. Mineralogical Magazine, 2017, 81, 1203-1222.	1.4	1
408	Estimating the resolution of real images. Journal of Physics: Conference Series, 2017, 849, 012042.	0.4	1
409	PB-06Three-dimensional Morphological Analysis of Supporting Tissues in the Dried Peduncle of Arabidopsis by X-ray Micro-CT. Microscopy (Oxford, England), 2018, 67, i34-i34.	1.5	1
410	Synchrotron Radiation Nanotomography of Biological Soft Tissues. Microscopy and Microanalysis, 2018, 24, 362-363.	0.4	1
411	Synchrotron radiation microtomography of brain hemisphere and spinal cord of a mouse model of multiple sclerosis revealed a correlation between capillary dilation and clinical score. Journal of Comparative Neurology, 2019, 527, 2091-2100.	1.6	1
412	High-Resolution Mapping of Local Photoluminescence Properties in CuO/Cu2O Semiconductor Bi-Layers by Using Synchrotron Radiation. Materials, 2021, 14, 5570.	2.9	1
413	Ray-tracing simulation and in-orbit performance of the ASTRO-H hard x-ray telescope (HXT). , 2016, , .		1
414	Application of Concentric Multilayers to Various X-ray Optical System. Shinku/Journal of the Vacuum Society of Japan, 2003, 46, 261-264.	0.2	1

#	Article	IF	CITATIONS
415	SPring-8ã«ãŠã'ã,‹é«~å^†è§£èƒ½Xç·šCTè£ç½® (XTM) ã®é−‹ç™ºãëãã®éš•石ã,ã®å¿œç". Ganseki Kobutsu Kagal	Ru, <b>2001,</b> ∶	30194-95.
416	High-Energy X-ray Activities at SPring-8. Synchrotron Radiation News, 2020, 33, 37-43.	0.8	1
417	Improved in-vivo airway gene transfer via magnetic-guidance, with protocol development informed by synchrotron imaging. Scientific Reports, 2022, 12, .	3.3	1
418	2P369 Microtomographic analysis of Drosophila brain(44. Neuro-biophysics,Poster) Tj ETQq0 0 0 rgBT /Overlock	10 Tf 50 6 0.1	522 Td (Sessi
419	Fabrication of Porous Aluminium and Copper Media by Using Monotectic Solidification under a Magnetic Field. Materials Science Forum, 2006, 512, 289-294.	0.3	0
420	698. Towards Non-Invasive Assessment of CF Airway Gene Therapy: High Resolution Propogation-Based Imaging of Airway Surface Liquid Via Synchrotron Light. Molecular Therapy, 2006, 13, S270.	8.2	0
421	Microfabric analysis of the surficial layer of deep-sea sediments by micro X-ray CT: an example from the Nansei-shoto (Ryukyu) Trench. Journal of the Geological Society of Japan, 2008, 114, III-IV.	0.6	0
422	The current status of reflector production and hard x-ray characterization for ASTRO-H/HXT. Proceedings of SPIE, 2011, , .	0.8	0
423	The Effect of Changing Positive End-Expiratory Pressures on the Spatial Pattern of Lung Ventilation in Newborn Rabbits Ventilated from Birth. Pediatric Research, 2011, 70, 45-45.	2.3	0
424	Towards a high-resolution local tomography using statistical iterative reconstruction. , 2011, , .		0
425	Visualization of neurons in the brain with phase-contrast CT. , 2012, , .		0
426	Development of diffraction-amalgamated grain-boundary tracking technique and its application to polycrystalline metals. Proceedings of SPIE, 2012, , .	0.8	0
427	<i>In Situ</i> Study of the Altering Globule Packing-Density during Semisolid Alloy Deformation. Solid State Phenomena, 0, 192-193, 185-190.	0.3	0
428	Nondestructive observation of fatigue crack propagation process in some solder joints by synchrotron radiation X-ray micro-tomography. , 2013, , .		0
429	Study of Creep Damage in a 10.86% Cr Heat Resistant Steel using Synchrotron X-Ray Microtomography. Advanced Materials Research, 2013, 794, 476-483.	0.3	0
430	Micro Scale Distribution of Nanoparticles Studied with X-ray Near-Field Scattering. Kobunshi Ronbunshu, 2014, 71, 580-585.	0.2	0
431	Development of 3D crystallographic orientation measurement for grain deformation analysis in aluminum alloy. Transactions of Nonferrous Metals Society of China, 2014, 24, 2094-2101.	4.2	0
432	Assessment of Deformation Behavior of Polycrystalline Aluminum Using Diffraction-Amalgamated Grain-Boundary Tracking (DAGT) Technique. Materials Science Forum, 0, 794-796, 57-62.	0.3	0

#	Article	IF	CITATIONS
433	Recent progress of X-ray tomography in material science field. Keikinzoku/Journal of Japan Institute of Light Metals, 2014, 64, 510-517.	0.4	0
434	X-ray Tomographic Microscopy of Drosophila Brain Network and Skeletonized Model Building in the Three-Dimensional Image. Microscopy and Microanalysis, 2015, 21, 917-918.	0.4	0
435	C2-O-05Non-destructive observation of aerenchyma development in the primary root of rice using X-ray micro-CT. Microscopy (Oxford, England), 2015, 64, i66.2-i66.	1.5	Ο
436	Imaging properties and its improvements of scanning/imaging x-ray microscope. AIP Conference Proceedings, 2016, , .	0.4	0
437	PB-03Folded structure of cell surface in dry seeds: real or artifact?. Microscopy (Oxford, England), 2016, 65, i25.1-i25.	1.5	0
438	PB-05Observation of Arabidopsis Roots Using X-ray Micro Computed Tomography. Microscopy (Oxford,) Tj ETQq	0 0 0 rgB <sup>-</sup> 1.5	[ /Qverlock 1
439	Spatial Resolution of Pre-reconstruction Raw Images and their Nano-CT Slices. Microscopy and Microanalysis, 2018, 24, 360-361.	0.4	Ο
440	Improvement of Scanning Procedure for 4D-X-ray Phase Tomography. Microscopy and Microanalysis, 2018, 24, 132-133.	0.4	0
441	Localized Photoluminescence Imaging of Bi-Layered Cuprous/Cupric Oxide Semiconductor Films by Synchrotron Radiation (Phys. Status Solidi B 3/2019). Physica Status Solidi (B): Basic Research, 2019, 256, 1970018.	1.5	Ο
442	Influence of hydrogen on stress corrosion cracking behavior in Al–10Mg alloy. Keikinzoku/Journal of Japan Institute of Light Metals, 2019, 69, 223-227.	0.4	0
443	Nanometer-Scale Structures of Neurons Differ Between Individuals and Those Differences Become Extraordinary in Schizophrenia. Microscopy and Microanalysis, 2019, 25, 1344-1345.	0.4	Ο
444	Optimization of Mechanical Properties in Aluminum Alloys <i>via</i> Hydrogen Partitioning Control. Tetsu-To-Hagane/Journal of the Iron and Steel Institute of Japan, 2019, 105, 240-253.	0.4	0
445	Tomographic reconstruction using tilted Laue analyser-based X-ray phase-contrast imaging. Journal of Synchrotron Radiation, 2021, 28, 283-291.	2.4	Ο
446	Assessment of Hydrogen Accumulation Behavior in Al–Zn–Mg Alloy under Strain with Kelvin Force Microscopy. Materials Transactions, 2021, 62, 636-641.	1.2	0
447	Can the changes in sediment concentration be recorded by the three-dimensional grain fabric in plane-bed deposits? :. Journal of the Sedimentological Society of Japan, 2007, 64, 111-115.	0.3	0
448	Application of Diffraction-Amalgamated Grain Boundary Tracking (DAGT) to Fatigue Crack Propagation Behavior in High Strength Aluminum Alloy. , 2014, , 91-96.		0
449	Nondestructive Observation of Thermal Fatigue Crack Propagation in FBGA and Die Attached Solder Joints by Synchrotron Radiation X-Ray Laminography. , 2015, , .		0
450	Transitional effect of 3D microstructural features on short crack growth behavior in Ti-6Al-4V alloy. The Proceedings of the Materials and Mechanics Conference, 2018, 2018, OS0110.	0.0	0

#	Article	IF	CITATIONS
451	Evaluation of Macroscopic Mechanical Properties from 3-D Visualization of Microstructure in Sintering. Funtai Oyobi Fummatsu Yakin/Journal of the Japan Society of Powder and Powder Metallurgy, 2019, 66, 604-610.	0.2	0
452	Assessment of 3D Short Crack Closure in Ti-6Al-4V Alloy Utilizing Synchrotron X-ray Microtomography. MATEC Web of Conferences, 2020, 321, 11051.	0.2	0
453	A Surrogate Approach to Reveal Microstructural Mechanisms Controlling the 3D Short Crack Growth in a Ti-6Al-4V Alloy. MATEC Web of Conferences, 2020, 321, 11004.	0.2	0
454	3-D Observation with Synchrotron Radiation X-ray CT. Materia Japan, 2022, 61, 65-71.	0.1	0